PNAS RESEARCH ARTICLE | CHEMISTRY

Achieving complete electrooxidation of ethanol by single atomic Rh decoration of Pt nanocubes

Qiaowan Chang[a,b,1], Youngmin Hong[c,1], Hye Jin Lee[c,1], Ji Hoon Lee[b,d,1], Damilola Ologunagba[e], Zhixiu Liang[f], Jeonghyeon Kim[c], Mi Ji Kim[c], Jong Wook Hong[g], Liang Song[f], Shyam Kattel[e,2], Zheng Chen[a,h,2], Jingguang G. Chen[b,i,2], and Sang-Il Choi[c,j,2]

Edited by Alexis Bell, University of California, Berkeley, CA; received June 30, 2021; accepted December 27, 2021

The development of single site electrocatalysts such as single-atom catalyst (SAC) has demonstrated the advantages of high precious metal utilization and tunable metal-support interfacial properties. However, the fundamental understanding of unalloyed single metal atom decorated on a metallic substrate is still lacking. Herein, we report unalloyed single atomic, partially oxidized Rh on the Pt nanocube surface as the electrocatalyst to completely oxidize ethanol to CO_2 at a record-low potential of 0.35 V. In situ X-ray absorption fine structure measurements and density functional theory calculations reveal that the single-atom Rh sites facilitate the C–C bond cleavage and the removal of the *CO intermediates. This work not only reveals the fundamental role of unalloyed, partially oxidized SAC in ethanol oxidation reaction but also offers a unique single-atom approach using low-coordination active sites on shape-controlled nanocatalysts to tune the activity and selectivity toward complicated catalytic reactions.

single atom catalyst | rhodium | platinum nanocubes | ethanol oxidation reaction

Heterogeneous electrocatalysts have received ever-increasing attention owing to global issues such as climate change and energy supply. Since platinum group metals such as Pt, Pd, Ir, Rh, and Ru are particularly active in electrocatalysis, their development as catalysts has been fundamentally established by single crystals (1–6) and practically proceeded with alloying (7, 8), surface defect engineering (9, 10), and nanocrystal synthesis (7, 11). Specifically, single-atom catalysts (SACs) have been prepared by coordinating single metal atoms with carbon-based supports or by embedding them into the defects in metal oxides/metal-organic frameworks (MOFs) to prevent the clustering (12, 13). However, drawbacks remain that carbon-supported SACs are significantly deactivated during the irreversible oxidation of carbon (14), and some of the single atoms completely embedded in metal oxides/MOFs cannot be activated (13).

Meanwhile, single-atom alloy (SAA) catalysts have been developed in which the surface of metallic substrates is atomically alloyed by dispersing trace amounts of other metals. As an example, Rh–Pt SAA decorated on a PtBi surface promoted activity and stability toward the ethanol oxidation reaction (EOR) (15). In addition, density functional theory (DFT) calculations predicted that the Rh–Pt SAA boosted the C–C bond cleavage owing to the strain and ligand effects. However, such Rh–Pt SAA catalysts with bimetallic configurations have not achieved a high selectivity for the complete oxidation of ethanol to CO_2, which is essential for ethanol fuel cells. In addition, the fundamental question has remained as to how an unalloyed, low-coordinated single metal atom decorated on a metallic substrate behaves as a catalyst.

Herein, we succeeded in the controlled synthesis of dispersing partially oxidized single Rh on the (100) surface of Pt nanocubes ($Rh_{at}O$-Pt NCs). As is known, the Pt(100) surface shows higher ethanol to CO_2 conversion compared to Pt(111) and Pt(110), but it prefers partial oxidation to form acetic acid (CH_3COOH) owing to the impeded kinetics of C–C bond cleavage (16). Therefore, EOR was tested for $Rh_{at}O$-Pt NCs to understand the unique role of $Rh_{at}O$ in enhancing the oxidization of ethanol to CO_2. Pt NCs decorated with partially oxidized Rh clusters ($Rh_{cl}O$-Pt NCs), Pt NCs, and commercial Pt/C were also prepared for comparison. The catalyst prepared after loading $Rh_{at}O$-Pt NCs on a carbon support ($Rh_{at}O$-Pt NCs/C) demonstrated the highest EOR activity among all prepared electrocatalysts. At 0.75 V (versus reversible hydrogen electrode [RHE]), $Rh_{at}O$-Pt NCs/C showed 1.5-, 4.2-, and 11.4-fold higher current density than those of $Rh_{cl}O$-Pt NCs/C, Pt NCs/C, and commercial Pt/C, respectively. Most importantly, the decoration of isolated $Rh_{at}O$ rendered the $Rh_{at}O$-Pt NCs/C electrocatalyst capable to break the C–C bond of ethanol, resulting in >99.9% of CO_2 selectivity in a record-low onset and wide potential region (0.35 to 0.75 V). In addition, in situ measurements, including infrared reflection absorption spectroscopy (IRRAS), X-ray absorption fine structure (XAFS), and DFT calculations, demonstrated that the single-atom Rh sites could facilitate the C–C

Significance

Direct ethanol fuel cells are attracting growing attention as portable power sources due to their advantages such as higher mass-energy density than hydrogen and less toxicity than methanol. However, it is challenging to achieve the complete electrooxidation to generate 12 electrons per ethanol, resulting in a low fuel utilization efficiency. This manuscript reports the complete ethanol electrooxidation by engineering efficient catalysts via single-atom modification. The combined electrochemical measurements, in situ characterization, and density functional theory calculations unravel synergistic effects of single Rh atoms and Pt nanocubes and identify reaction pathways leading to the selective C–C bond cleavage to oxidize ethanol to CO_2. This study provides a unique single-atom approach to tune the activity and selectivity toward complicated electrocatalytic reactions.

Author contributions: Q.C., Z.C., J.G.C., and S.-I.C. designed research; Q.C., Y.H., H.J.L., J.H.L., D.O., Z.L., J.K., M.J.K., L.S., and S.K. performed research; J.W.H. contributed new reagents/analytic tools; Q.C., J.H.L., D.O., and S.K. analyzed data; and Q.C., Y.H., H.J.L., J.H.L., D.O., S.K., Z.C., J.G.C., and S.-I.C. wrote the paper.

The authors declare no competing interest.

This article is a PNAS Direct Submission.

[1]Q.C., Y.H., H.J.L., and J.H.L. contributed equally to this work.

[2]To whom correspondence may be addressed. Email: shyam.kattel@famu.edu, zhengchen@eng.ucsd.edu, jgchen@columbia.edu, or sichoi@knu.ac.kr.

This article contains supporting information online at http://www.pnas.org/lookup/suppl/doi:10.1073/pnas.2112109119/-/DCSupplemental.

Published March 9, 2022.

bond cleavage and the removal of the *CO intermediate, promoting EOR performances. Our work demonstrated partially oxidized Rh_{at}-O active sites as a unique SAC on shape-controlled nanocatalysts that can dramatically enhance the catalytic activity and selectivity compared with conventional nanocatalysts in complicated reactions such as EOR.

Results and Discussion

The $Rh_{at}O$-Pt NCs/C catalysts were prepared from a two-step solution method, with Pt NCs/C being prepared first as the substrate for further Rh decoration. During the synthesis of Pt NCs, CO gas was used directly instead of the common capping agent such as metal carbonyls to avoid the pollution of trace amount of metal (8). The transmission electron microscopy (TEM) image in *SI Appendix*, Fig. S1*A* showed the as-prepared Pt NCs with an average edge length of 10.8 ± 1.0 nm. These NCs can be uniformly dispersed on carbon to form the final electrocatlysts (Pt NCs/C, *SI Appendix*, Fig. S1*B*). The atomic level decoration of Rh on Pt NCs/C was achieved by adding a trace amount of Rh precursors [Rh(III) acetylacetonate or $Rh(acac)_3$] in the organic mixture containing Pt NCs/C (see *Materials and Methods* for details). In order to thermally decompose the metal–ligand bonds in $Rh(acac)_3$, an annealing temperature of 250 °C was applied. In addition, this annealing condition was sufficient to prevent the clustering of Rh atoms because of the high surface free energy and the Rh–Rh interatomic bond energy (93 kJ · mol^{-1}) (17, 18). Therefore, we expect that the thermally decomposed Rh atoms favor a single-atom distribution rather than cluster or particle growth on the surface of Pt NCs. By adding twice the amount of Rh precursor using a similar procedure, $Rh_{cl}O$-Pt NCs were obtained. After the Rh decoration, the cubic morphologies were maintained with average edge lengths of 10.4 ± 1.2 and 10.9 ± 1.3 nm for $Rh_{at}O$-Pt NCs/C and $Rh_{cl}O$-Pt NCs/C, respectively (*SI Appendix*, Fig. S1 *C* and *D*). The same *d*-spacings of the Pt(200) plane (0.196 nm) were observed for $Rh_{at}O$-Pt NCs/C and $Rh_{cl}O$-Pt NCs/C, suggesting the nonalloy formation during the decoration process (Fig. 1 *A* and *B*). The high-angle annular dark-field–scanning TEM (STEM) with energy dispersive X-ray spectroscopy (EDS) elemental mapping images of $Rh_{at}O$-Pt NCs/C and $Rh_{cl}O$-Pt NCs/C represent the weak Rh signals in the outer layer of Pt NCs (white dots region in Fig. 1 *A* and *B*), suggesting that Rh was distributed on the surface of Pt NCs without the formation of the Rh shell. The O signals are evenly distributed over the single cubes, revealing the presence of oxygen in both samples. To further examine the decorated structure of $Rh_{cl}O$-Pt NCs/C, STEM–EDS line scans were conducted at five different locations on a single $Rh_{cl}O$-Pt NC (*SI Appendix*, Fig. S2). As marked by the black arrows in *SI Appendix*, Fig. S2*B*, some EDS line profiles showed Rh signals at the edges, while others did not, indicating the presence of Rh clusters on Pt NC but not a complete coating of Rh shell. X-ray diffraction (XRD) patterns did not show any shift in the Pt peak position, suggesting that Pt and Rh did not form alloys in the Rh-modified Pt NCs/C samples (*SI Appendix*, Fig. S3). The chemical states of Pt and Rh were identified by X-ray photoelectron spectroscopy (XPS). Both Pt and Rh were in the oxidized form as indicated by the presence of Pt(II) in the deconvoluted 4*f* peaks and positively shifted Rh 3*p* peaks in both samples (*SI Appendix*, Fig. S4). The quantitative Pt-to-Rh ratios of samples were determined by inductively coupled plasma-atomic emission spectroscopy (ICP-AES), suggesting stoichiometric composition of $Rh_1Pt_{19.8}$ and $Rh_1Pt_{11.4}$ for $Rh_{at}O$-Pt NCs/C and $Rh_{cl}O$-Pt NCs/C, respectively (*SI Appendix*, Table S1). Also, based on the ICP-AES results and the particle size of Pt NCs (*SI Appendix*, Table S1), about 33% of the Pt surface was decorated with Rh atoms in $Rh_{at}O$-Pt NCs/C, but the Rh_{cl} coverage was not quantified because of the clustering of Rh atoms on the Pt surface in the $Rh_{cl}O$-Pt NCs/C sample.

To further explore the coordination structure and the nature of Rh decoration in both samples, XAFS measurements were carried out. The X-ray absorption near edge structure (XANES) and Fourier-transformed extended XAFS (EXAFS) profiles of Pt (*SI Appendix*, Fig. S5 *A*, *C*, and *D* and Tables S2–S4) indicated the absence of Pt–Rh alloying signal in both samples (19). Different from the XPS results, the nearly identical XANES spectra of samples and the Pt foil revealed the metallic status of Pt in the bulk. Therefore, it could be concluded that only surface Pt was oxidized to a certain extent since XPS is a surface-sensitive technique. Unlike in the Pt L_3-edge, the XANES profiles of Rh K-edge (*SI Appendix*, Fig. S5*B*) represented the average Rh oxidation state of samples in the order of Rh foil < $Rh_{cl}O$ < $Rh_{at}O$ < Rh_2O_3. EXAFS profiles at the Rh K-edge displayed distinguishable features from those of the Rh foil. The strong peak near ∼1.5 Å and the absence of the Rh–Pt peak in the EXAFS profile (Fig. 1 *C* and *D* and *SI Appendix*, Fig. S6) were attributed to the presence of oxidized Rh atoms, indicating that Rh atoms were preferentially located on the aforementioned oxygen atoms on the Pt NC surfaces. In addition, there was no Rh–Rh peak for Rh_{at}-Pt NCs/C, confirming the success of our synthetic approach for atomically dispersed Rh on the surface of Pt NCs. While $Rh_{at}O$-Pt NCs/C exclusively revealed the Rh–O–Pt bonding with its coordination number of 3.2(6) (*SI Appendix*, Table S5), $Rh_{cl}O$-Pt NCs/C displayed both Rh–O–Pt and metallic Rh–Rh bonding with their coordination numbers being 1.7(1) and 1.7(3), respectively (*SI Appendix*, Table S6). The presence of the latter bonding could be verified by the peak near ∼2.6 Å (Fig. 1*D*). These Rh coordination data are in good agreement with the Rh oxidation trend obtained by XANES. Based on the XAFS observations, expected surface models were illustrated for $Rh_{at}O$-Pt NC and $Rh_{cl}O$-Pt NC (Fig. 1 *E* and *F*), showing that the $Rh_{at}O$-Pt NCs can provide high accessibility in an open structure.

The cyclic voltammetry (CV) test also revealed different surface properties of the prepared electrocatalysts (Fig. 2*A*). The Pt(100) surface of Pt NCs/C was identified by the typical H adsorption/desorption features (0.08 to 0.45 V versus RHE) of single crystal Pt(100) shown in its CV curves (20). The distinct surface elemental distributions of $Rh_{at}O$-Pt NCs/C and $Rh_{cl}O$-Pt NCs/C were represented by the reduction peaks of M–O (M = Pt or Rh). The cathodic CV curve of $Rh_{at}O$-Pt NCs/C showed the reduction of Pt-O (0.75 to 1.0 V) and Rh-O (0.45 to 0.65 V) peaks, confirming that both Pt and Rh were present on the surface. For $Rh_{cl}O$-Pt NCs/C, the absence of an obvious reduction peak of Pt–O implied an Rh-dominated surface because of the decoration of Rh clusters.

The preferentially exposed Pt(100) facets of Pt NCs/C are active toward EOR, presented by the negatively shifted onset potential of 200 mV in comparison with Pt/C (Fig. 2*B* and *SI Appendix*, Fig. S7). However, the enhancement in terms of current densities was limited, with the current density of Pt NCs being only 2.7-fold higher than that of commercial Pt/C at 0.75 V. After Rh decoration, not only the EOR overpotentials further reduced but also the current densities showed significant enhancement. For example, compared to Pt/C, $Rh_{at}O$-Pt NCs/

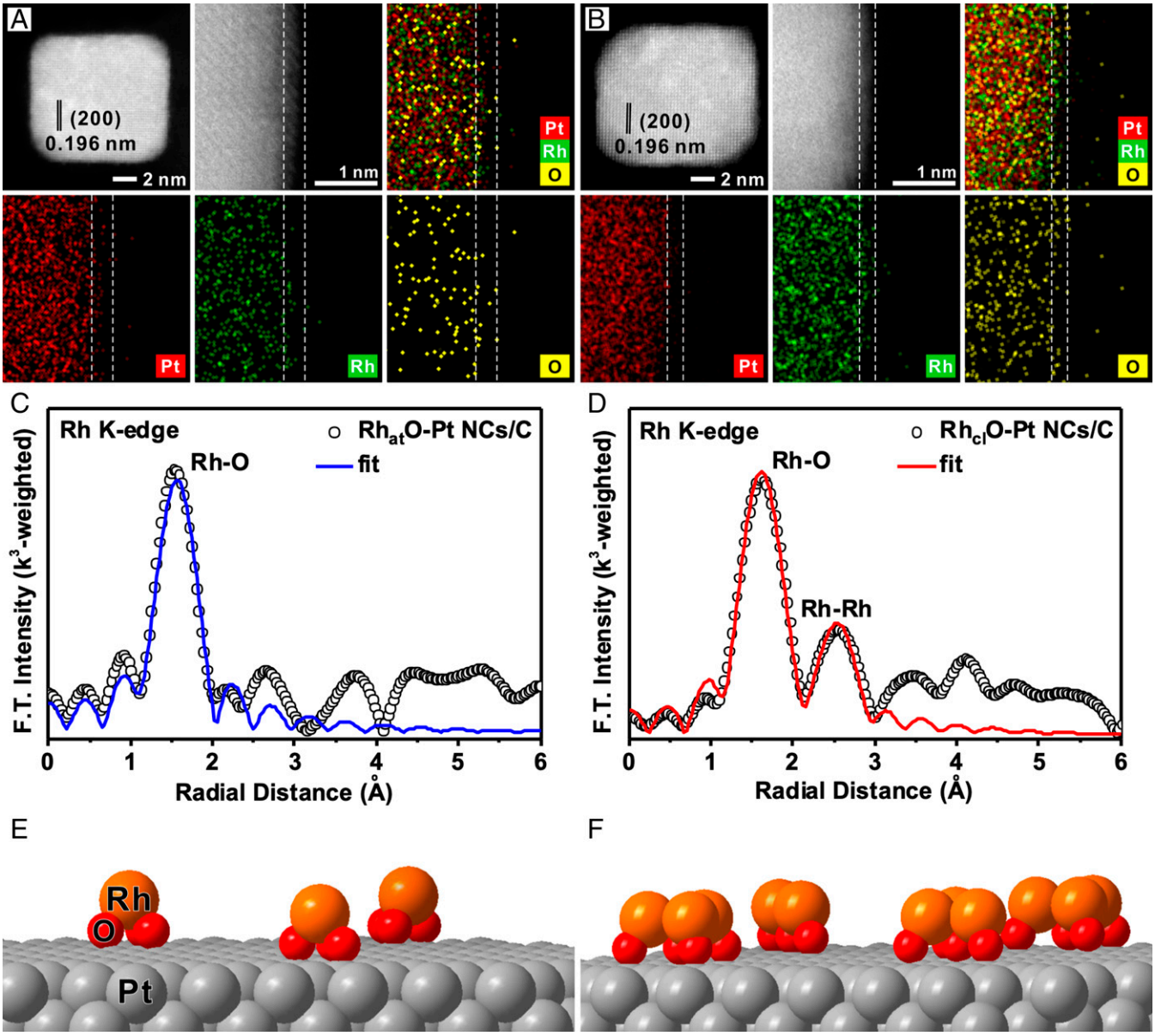

Fig. 1. High-angle annular dark-field STEM images and EDS mapping image of (*A*) $Rh_{at}O$-Pt NCs and (*B*) $Rh_{cl}O$-Pt NCs. The k^3-weighted Rh K-edge EXAFS spectra of (*C*) $Rh_{at}O$-Pt NCs/C and (*D*) $Rh_{cl}O$-Pt NCs/C. Schematic models of (*E*) $Rh_{at}O$ and (*F*) $Rh_{cl}O$ decorated Pt surface.

C showed more negative shifts of the EOR onset and main peak potentials by 350 and 85 mV, respectively (Fig. 2*B*). Furthermore, the EOR current densities of $Rh_{at}O$-Pt NCs/C and $Rh_{cl}O$-Pt NCs/C showed 11.4- and 7.7-fold enhancement over Pt/C at 0.75 V, respectively (Fig. 2*C*). The chronoamperometric test also showed the same EOR activity trend among the electrocatalysts: Pt/C < Pt NCs/C < $Rh_{cl}O$-Pt NCs/C < $Rh_{at}O$-Pt NCs/C at 0.65 V (*SI Appendix*, Fig. S8). As for the decoration effect, $Rh_{at}O$ is better for EOR than $Rh_{cl}O$. To explore the reasons, Rh nanocubes/C (Rh NCs/C) and Rh NCs with decorated Pt clusters (Pt_{cl}-Rh NCs/C) were prepared. Rh NCs/C was relatively inactive for EOR, but the EOR activity of $Pt_{cl}O$-Rh NCs/C was enhanced by 83% after the deposition of Pt clusters, indicating that the EOR activity is mainly from Pt rather than Rh (*SI Appendix*, Fig. S9). Then the activity enhancement from the $Rh_{at}O$ and $Rh_{cl}O$ could be attributed to the Rh–O bonds, which might facilitate the formation of adsorbed OH species to remove the strongly adsorbed *CO during the EOR. Moreover, the $Rh_{at}O$ single-atomic dispersion renders the corresponding catalyst the highest utilization of Rh–O active sites, making full use of Rh atoms. The stability of $Rh_{at}O$-Pt NCs/C was examined by a prolonged chronoamperometric test at 0.55 V for every 10,000 s followed by the CV cleaning scans (*SI Appendix*, Fig. S10). After CV cleaning to remove the poisoned intermediates, the current density of $Rh_{at}O$-Pt NCs/C could be recovered during each chronoamperometric test. After 30,000 s, the maximum current density of $Rh_{at}O$-Pt NCs/C from CV curves only decreased by 8% (Fig. 2*D*), showing a superior stability to Pt/C (decreased by 35%).

The advantage of $Rh_{at}O$ decoration is more prominent for improving the ethanol fuel utilization by completely oxidizing ethanol to CO_2. From in situ IRRAS measurements, four important intermediates and products were identified, CO (linearly adsorbed CO_L, 2,050 cm^{-1}), CO_2 (asymmetric stretching, 2,341 cm^{-1}), CH_3CHO (933 cm^{-1} as a representative peak), and CH_3COOH (1,280 cm^{-1} as a representative peak) (Fig. 3 and *SI Appendix*, Table S7) (21). The onset potential

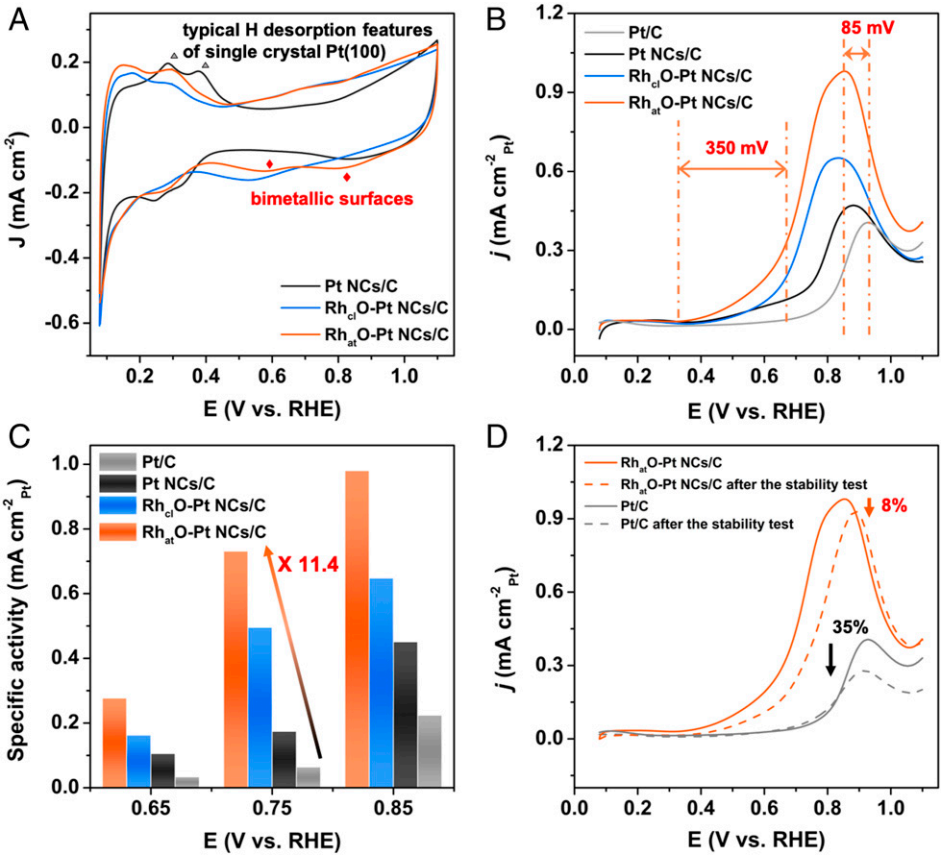

Fig. 2. (*A*) CV curves of the prepared electrocatalysts in Ar-saturated 0.1 M $HClO_4$ solution. (*B*) Anodic polarization EOR curves for electrocatalysts in Ar-saturated 0.1 M $HClO_4$ + 0.2 M ethanol solution with a scan rate of 50 mV · s^{-1}. (*C*) Specific activity measured at different potentials of electrocatalysts. (*D*) The anodic CV curves of $Rh_{at}O$-Pt NCs/C and Pt/C before and after the stability test. The current densities are normalized to the electrochemical surface area.

for CO_2 formation is an indicator of the ability of the electrocatalyst to break the C–C bond and the subsequent oxidation of adsorbed CO. The potential for the initial generation of CO_2 over different electrocatalysts followed the order: $Rh_{at}O$-Pt NCs/C (0.35 V) < $Rh_{cl}O$-Pt NCs/C (0.45 V) < Pt NCs/C (0.55 V) < commercial Pt/C (0.65 V). The CO_2 generation potential of $Rh_{at}O$-Pt NCs/C was the closest to the thermodynamic potential for the oxidation of ethanol to CO_2 (0.143 V) among the Pt-based electrocatalysts in the literature (*SI Appendix*, Table S8), demonstrating its high activity to break the C–C bond. Besides, the peak located at 1,705 to 1,706 cm^{-1} represents the C = O stretching of C2 products (CH_3CHO and CH_3COOH). As shown in Fig. 3*A*, even at 1.05 V, the IRRAS spectra of $Rh_{at}O$-Pt NCs/C still showed the negligible peak of 1,705 to 1,706 cm^{-1}, suggesting that only a trace amount of C2 products were produced during the EOR. In addition, liquid products at the completion of electrolysis at 0.85 V_{RHE} and 1.05 V_{RHE} for 1 h were quantified by using high-performance liquid chromatography (HPLC) (see details in *Materials and Methods*). The Faradaic efficiency toward CH_3COOH was presented in *SI Appendix*, Fig. S11, showing a consistent trend with that from the IRRAS measurements.

The distribution of different EOR products were quantitatively determined from 0.35 to 1.05 V via the peak integration method developed by Weaver et al. (22) (Fig. 3*E* and *SI Appendix*, Fig. S12). Consistent with previous reports, the main product for Pt NCs/C and Pt/C was CH_3COOH, and Pt NCs/C presented a higher CO_2 selectivity than Pt/C (17.0 versus 2.4% at 1.05 V) (23, 24). It was noted that the CO_2 selectivity of Pt NCs/C was much higher than the previous study using $W(CO)_6$ to synthesize Pt NCs, confirming the importance of a clean Pt surface without trace amounts of W metal in EOR (7, 8). The Rh decoration remarkably improved the CO_2 selectivity. The $Rh_{at}O$-Pt NCs/C catalyst exhibited >99.9% CO_2 selectivity from 0.35 to 0.75 V, demonstrating its strong ability to break the C–C bond of ethanol in a wide potential range. We believe this is the first case that can achieve complete oxidation of ethanol to CO_2 in such a wide potential range. The CO_2 selectivity of $Rh_{at}O$-Pt NCs/C is still very high after 0.75 V, such as 32% of CO_2 selectivity at 1.05 V. Consistent with the trend in EOR activity, the $Rh_{at}O$ decoration is better than the $Rh_{cl}O$ on Pt NCs for the C–C bond scission in ethanol.

Specifically, the role of Rh in breaking the C–C bond was also evidenced by the in situ IRRAS spectra of Rh NCs/C and Pt_{cl}-Rh NCs/C (*SI Appendix*, Fig. S13). For Rh NCs/C, despite its low activity, a CO_2 peak was generated at the beginning of the EOR (0.15 V) without the detection of adsorbed CO. While for Pt_{cl}-Rh NCs/C, the CO_2 peak was visible from 0.55 V, and the CO peak was formed from 0.35 V. Thus, the roles of Rh and Pt in EOR appear to be different, with Rh being the active component to break the C–C bond in ethanol and Pt as the active center for the overall EOR activity. Therefore, Rh–O–Pt can combine the activity of Rh and Pt and additionally assist the formation of surface OH to remove the poisoning *CO as confirmed in the CO stripping analysis (*SI Appendix*, Fig. S14). The oxidation of CO began in the order of $Rh_{at}O$-Pt NCs/C, $Rh_{cl}O$-Pt NCs/C, Pt NCs/C, and commercial Pt/C, presenting the higher capability of $Rh_{at}O$-Pt NCs/C to oxidized *CO. These results suggest the unique role

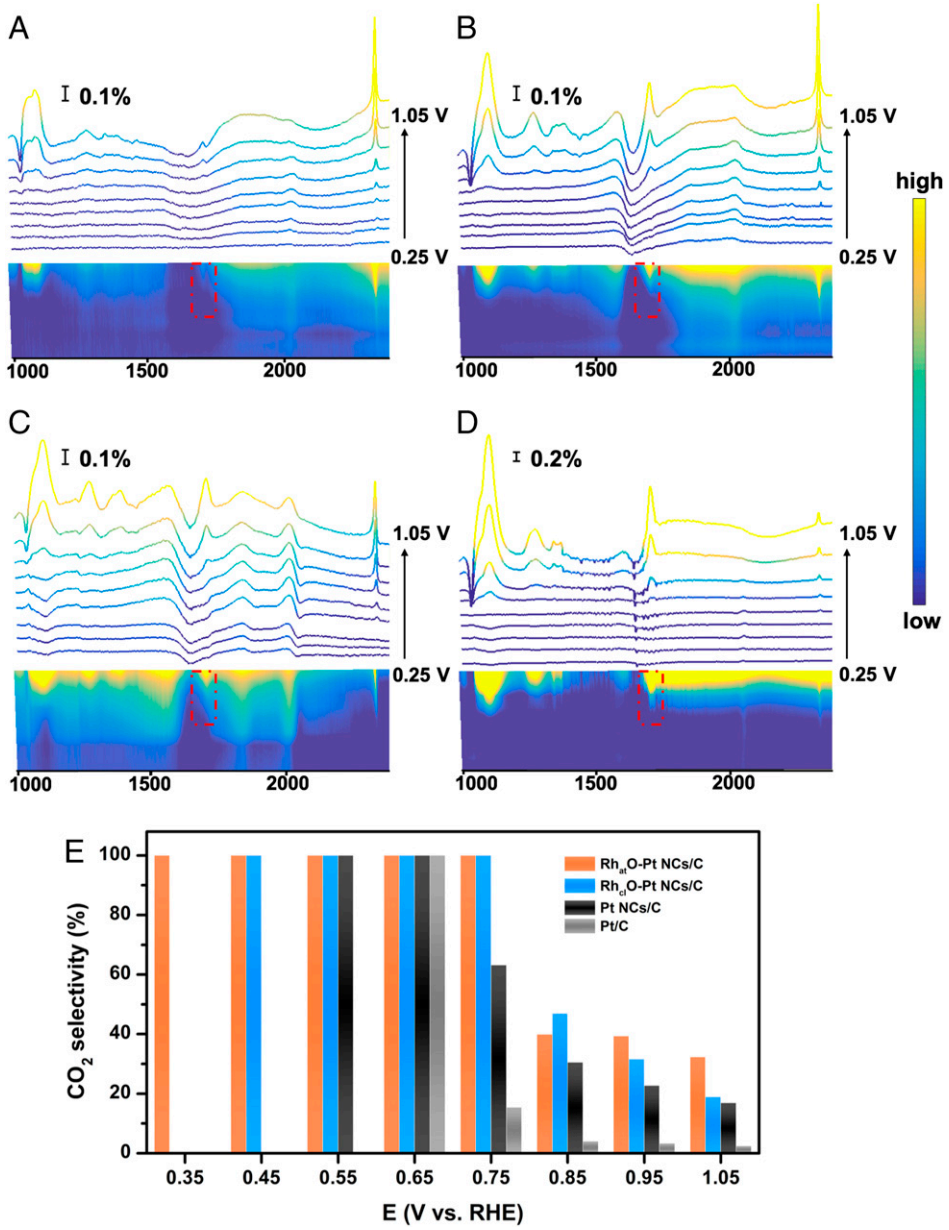

Fig. 3. Recorded in situ IRRAS spectra during CV test from 0.25 to 1.05 V on (*A*) $Rh_{at}O$-Pt NCs/C, (*B*) $Rh_{cl}O$-Pt NCs/C, (*C*) Pt NCs/C, and (*D*) commercial Pt/C in 0.1 M $HClO_4$ + 0.2 M ethanol solution. The red dot regions highlighted the projection files of the peak at 1,705 to 1,706 cm^{-1}. (*E*) The calculated CO_2 selectivity of all samples from 0.25 to 1.05 V.

of the single $Rh_{at}O$ decoration on a shape-controlled electrocatalyst to effectively break the C–C bond and the subsequent oxidation of *CO.

Based on the electrochemical and in situ IRRAS results, the unprecedented EOR selectivity of $Rh_{at}O$-Pt NCs/C suggests a unique environment of $Rh_{at}O$ on the Pt(100) surfaces as a new active site. In order to verify the catalysis behavior of $Rh_{at}O$-Pt NCs/C, in situ XAFS analysis was conducted at the Rh K-edge using the chronoamperometric mode of EOR at 0.75 V. When comparing the XANES profiles, the oxidation state of Rh was apparently reduced during the chronoamperometric measurements (Fig. 4*A*). This result reveals that the reaction intermediates such as *CO and $*CH_3CH_2CO$ donate their electrons to $Rh_{at}O$ to form a sigma (σ) bond. The σ bond formation on the $Rh_{at}O$ site was further confirmed in the EXAFS profiles by the onset of a new intense peak in the range of 1∼1.5 Å (Fig. 4*B*). At the same time, the peak for the Rh–O bond shifted toward higher *R* values (2.00∼2.20 Å), indicating an extended Rh–O bond because of the partial reduction of Rh.

In general, such σ bond formation between Rh and intermediates is not surprising as observed in transition metal carbonyl complexes (25–27). In addition, a similar reaction configuration was observed that an intermediate Rh–C bond was formed in RhCo-MCM-41 during the reaction between CO_2 and ethane to yield C3 products (28). However, in the present work, EXAFS signals surprisingly recovered back to the pristine profile upon the open circuit voltage condition after the chronoamperometric measurement, indicating the robust structural feature of the $Rh_{at}O$ site on the Pt NCs over the prolonged EOR period. Especially, the removal of the intermediate Rh–C bond led to the shrinkage of the Rh–O bond to the original value (∼1.5 Å), which indicates that the $Rh_{at}O$ site can adopt the reversible configuration of Rh–O and C–Rh–O bonds under pristine and reaction conditions, respectively, without significant energy penalties.

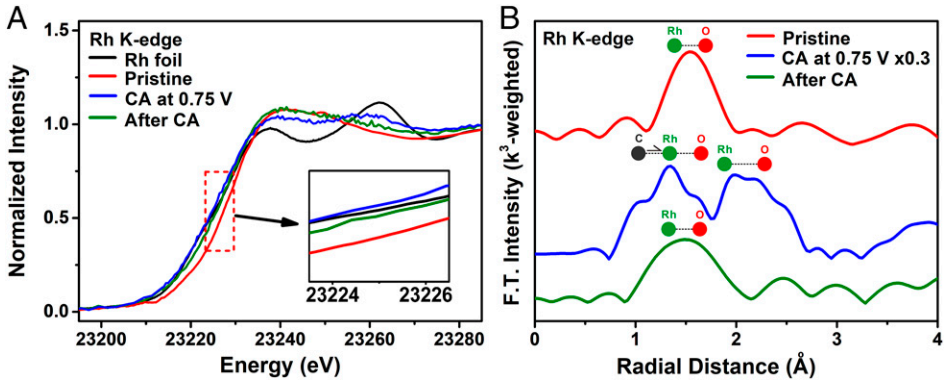

Fig. 4. (*A*) XANES and (*B*) EXAFS spectra for the Rh K-edge of Rh_{at}-O Pt NCs/C before, after, and during EOR chronoamperometric test in 0.1 M $HClO_4$ + 1.0 M ethanol solution at 0.75 V. As shown in the linear combination fitting results of XANES in *SI Appendix*, Fig. S15, the average oxidation state of Rh before and during EOR is approximately +1.7 and +1.0, respectively.

Adzic et al. (21) previously investigated an efficient catalyst composed of Pt–Rh–SnO_2 supported by carbon black (Pt–Rh–SnO_x/C), which showed a beneficial role of SnO_2 in strongly adsorbing water and interacting with Pt and Rh to form M–OH as well as the Pt–Rh alloy effect in promoting C–C bond cleavage. Our work provides a strategy by utilizing single-atom Rh to promote the complete EOR with optimized utilization of Rh without requiring the SnO_x component.

In situ IRRAS and XAFS results confirmed that the partially oxidized $Rh_{at}O$ sites serve as a robust catalytic active site for EOR and play an important role in the complete oxidation of ethanol. To gain further insight into the role of $Rh_{at}O$ in EOR, DFT calculations were performed to calculate the free energy change (ΔG) of C–C bond cleavage of CH_3CH_2OH along various possible pathways and the activation energy for the removal of *CO. The DFT-calculated binding energies (BEs) of intermediates in their most stable configurations show that $Rh_{at}O$/Pt(100) enhances the adsorption of CH_3CH_2OH, which should lead to a facilitated rate of CH_3CH_2OH conversion (*SI Appendix*, Fig. S16 and Table S9). However, most other intermediates bind weakly on $Rh_{at}O$/Pt(100) compared to Pt(100), leading to a higher tolerance of $Rh_{at}O$ single sites toward these species. The DFT obtained results on $Rh_{at}O$/Pt(100) in Fig. 5*A* show that the C–C bond scission occurs when the $*CH_3CO$ intermediate is formed via three sequential dehydrogenation steps: $*CH_3CH_2OH \longrightarrow *CH_3CHOH + 1/2H_2(g)$, $*CH_3CHOH \longrightarrow *CH_3COH + 1/2H_2(g)$, and $*CH_3COH \longrightarrow *CH_3CO + 1/2H_2(g)$. This pathway on $Rh_{at}O$/Pt(100) is similar to the DFT-predicted pathways on Rh surfaces by Hu et al. (29). However, the C–C bond cleavage differs from the pathway reported on Pt/Rh/SnO_2 in which the C–C bond cleavage is found to be facilitated via the formation of the $*CH_2CH_2O$ intermediate (21). A similar reaction pathway for the C–C bond cleavage is predicted on Pt(100) (*SI Appendix*, Fig. S17). Fig. 5*A* also shows that the potential limiting step: $*CH_3CH_2OH \longrightarrow *CH_3CHOH + 1/2H_2(g)$ along the most favorable pathways of C–C bond cleavage on $Rh_{at}O$/Pt(100) has a ΔG of 0.27 eV, which is comparable to a value of 0.14 eV predicted on Pt(100) (*SI Appendix*, Fig. S18).

Furthermore, CO binding is found to be significantly weakened on the $Rh_{at}O$/Pt(100) site compared to the sites on Pt(100) (*SI Appendix*, Table S9). Additional transition state calculations were performed to compute the activation energy (E_a) of OH-assisted *CO oxidation to $*CO_2$ (i.e., *HOCO formation: $*CO + *OH \longrightarrow *HOCO$ followed by *HOCO dissociation: $*HOCO + * \longrightarrow *CO_2 + *H$). The DFT-calculated E_a values of *HOCO formation and its dissociation were 0.72 and 0.24 eV, respectively, on $Rh_{at}O$/Pt(100), which were smaller than the corresponding values on Pt(100) of 0.92 and 0.94 eV, respectively. Therefore, consistent with the experimental observation, the DFT calculations predict the thermodynamically favorable C–C bond cleavage of $*CH_3CO$ to form $*CH_3$ + *CO intermediates on $Rh_{at}O$/Pt(100) at moderate applied potentials as well as the facile removal of *CO, enhancing the complete oxidation of ethanol to CO_2.

Because in situ XANES results (Fig. 4) suggested that Rh should be in the partially oxidized state during EOR, additional DFT calculations were performed on $Rh_{at}O$/Pt(100) and Rh_{at}/Pt(100) surfaces with different Bader charges (*SI Appendix*, Fig. S19 and

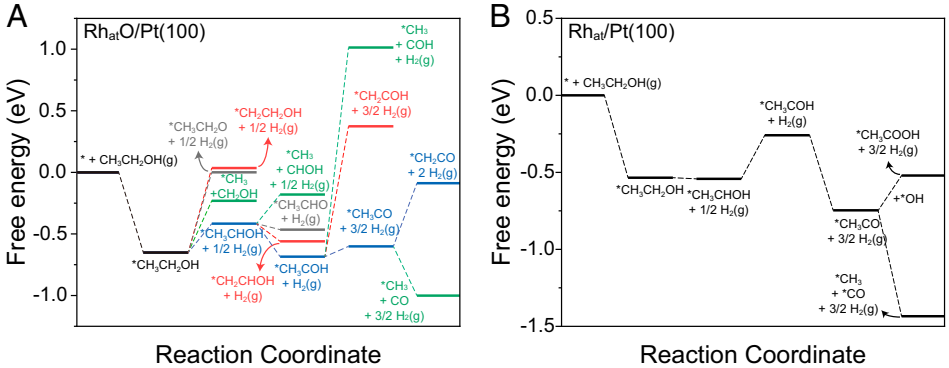

Fig. 5. DFT-calculated free energy profile of C–C bond cleavage of CH_3CH_2OH on (*A*) $Rh_{at}O$/Pt(100) and (*B*) Rh_{at}/Pt(100). As shown in the Bader charge analysis in *SI Appendix*, Fig. S19, the average oxidation state of Rh in *A* and *B* is approximately +1.2 and +0.1, respectively.

Fig. 5*B*). As shown in the linear combination fitting results of XANES in *SI Appendix*, Fig. S15, the average oxidation state of Rh is reduced from +1.7 in the pristine sample to +1.0 during EOR, indicating that a partially oxidized Rh state is responsible for the high EOR activity. DFT results (Fig. 5) reveal similar C–C bond cleavage pathways over $Rh_{at}O$/Pt(100) and Rh_{at}/Pt(100) surfaces and all the steps are predicted to be downhill in energy at moderate potential. Furthermore, the comparison of DFT results over surfaces with different Bader charges (*SI Appendix*, Fig. S19) illustrates that the C–C bond scission pathway, based on the difference in ΔG between the C–C bond scission of $*CH_3CO$ and its oxidation to acetic acid, becomes more favored as Rh is less oxidized, consistent with the experimental observation of C–C bond scission being preferred over acetic acid production.

Conclusions

In summary, we demonstrated that the decoration of single atomic $Rh_{at}O$ on the metallic Pt(100) surface notably enhances the C–C cleavage and *CO oxidation to achieve completely oxidizing ethanol to CO_2. The $Rh_{at}O$-Pt NCs/C presented 11.4-fold current density of Pt/C at 0.75 V and >99.9% of CO_2 selectivity in a wide potential range of 0.35 to 0.75 V. Our studies revealed that the single-atomic $Rh_{at}O$ sites could exploit particular advantages through the reversible configuration of Rh–O and C–Rh–O bonds during EOR: boosting the C–C bond cleavage to facilitate the conversion of ethanol and enhancing the formation of adsorbed -OH to remove the poisoning *CO. This work provided not only a fundamental understanding of the catalytic behavior of partially oxidized single Rh atoms on the Pt substrates to achieve the complete oxidation of ethanol to CO_2 but also a unique single-atom approach using low-coordination active sites to tune the activity and selectivity toward other electrocatalytic reactions.

Materials and Methods

Materials. Platinum(II) acetylacetonate [$Pt(acac)_2$, Pt 48.0%] was obtained from Alfa Aesar. Rhodium(III) acetylacetonate [$Rh(acac)_3$, 97%], oleic acid (OAc, 90%), oleylamine (OAm, 70%), benzyl alcohol (≥99%), and benzyl ether (98%) were obtained from Sigma-Aldrich. All chemicals were used as received without further treatment.

Synthesis of Pt NCs. In a standard synthesis, $Pt(acac)_2$ (0.102 mmol), OAc (2.0 mL), OAm (4.0 mL), and benzyl ether (14.0 mL) were added in a glass vial with a magnetic stirring bar. The mixture was heated to 130 °C under an Ar atmosphere. When the temperature reached 130 °C, CO gas was bubbled into the mixture with a flow rate of 30 mL · min^{-1}, and Ar purging was stopped at the same time. The mixture was then heated to 210 °C at a heating rate of 8 °C min^{-1} under CO gas and held at 210 °C for 40 min without CO gas bubbling. The resulting suspension was cooled down to room temperature naturally, and the Pt NCs were precipitated out by sequential addition of toluene (10 mL) and ethanol (15 mL). The supernatant was discarded by centrifugation at 3,000 rpm for 5 min. The resulting Pt NCs were dispersed in toluene for further treatment.

Preparation of Pt NCs/C. A suspension of Pt NCs was added into a toluene solution containing 40 mg Vulcan XC-72R carbon and kept under ultrasonic wave agitation for 30 min. The resulting Pt NCs/C catalyst was centrifuged three times with toluene at 3,000 rpm for 5 min and then dried under Ar protection at room temperature.

Synthesis of Rh-Decorated Pt NCs/C. As-prepared Pt NCs/C (20 mg), OAm (5 mL), and benzyl ether (5 mL) were added in a glass vial with a magnetic bar with a magnetic stirring bar. The mixture was heated to 250 °C under an Ar atmosphere. $Rh(acac)_3$ dissolved in benzyl ether (1 mL) was injected in a reaction mixture. The amount of $Rh(acac)_3$ was 1 mg (0.002 mmol) for a single $Rh_{at}O$-Pt NCs and was 2 mg (0.005 mmol) for $Rh_{cl}O$-Pt NCs. Then, the reaction mixture was maintained at 250 °C for 1 h. The resulting product was cooled down to room temperature naturally, and the Rh-decorated Pt NCs/C catalysts were centrifuged three times with toluene at 3,000 rpm for 5 min and then dried under Ar protection at room temperature. The surface coverage of Pt NCs/C by Rh atoms for $Rh_{at}O$-Pt NCs/C was calculated using the following equation:

$$\frac{\textit{The number of Rh atoms}}{\textit{The number of Pt atoms on the surface of Pt NCs/C}} \times 100(\%).$$

Morphological, Structural, and Elemental Characterization. TEM images were obtained using an H-7100 microscope (Hitachi) operated at an acceleration voltage of 120 kV. High-resolution TEM and EDS studies were carried out in a JEM-2100F (JEOL) and Titan G2 ChemiSTEM Cs Probe (FEI) operated at an acceleration voltage of 200 kV. The metal contents in catalysts were determined using ICP optical emission spectroscopy (PerkinElmer, Optima 7300DV) and ICP mass spectrometry (PerkinElmer, NexION 300×). XRD patterns were obtained with a D2 phaser X-ray diffractometer (Bruker). XPS was carried out using a spectrometer (Thermo Fisher Scientific) with Al Kα X-ray (1,486.6 eV) as the light source. All XPS spectra were aligned using the C1s peak at 284.8 eV as reference.

Electrochemical Measurements. The electrocatalyst ink was prepared by dispersing 2.0 mg electrocatalysts in the mixed 2 mL Milli-Q water and isopropanol solution (Milli-Q water: isopropanol = 4: 1) and 8 μl Nafion (5%). A total of 10 μl electrocatalyst ink was used for the electrochemical test. Glassy carbon, graphite rod, and Ag/AgCl (3 M · Cl^-) were used as the working, counter, and reference electrodes, respectively. All the potentials were calibrated to an RHE. To obtain the stable electrochemical result, 20 fast CV cycles were scanned first in Ar-saturated 0.1 M $HClO_4$ solution at 100 mV · s^{-1} in the range of 0.05 to 1.20 V (versus RHE). The CV curves were then recorded in 0.1 M $HClO_4$ solution with a scanning rate of 50 mV · s^{-1}. The EOR activities were measured in Ar-saturated 0.1 M $HClO_4$ and 0.2 M C_2H_5OH solution. The EOR CV curves were obtained with a scanning rate of 50 mV · s^{-1}. The chronoamperometric curves were measured at 0.65 V. For CO stripping tests, CO was adsorpted on the electrocatalyst surface by holding the potential at 0.05 V for 10 min in CO-saturated 0.1 M $HClO_4$ solution. The CO stripping curves were obtained after purging Ar for 30 min with a scanning rate of 50 mV · s^{-1}. The stability test was performed by a prolong chronoamperometric test at 0.55 V for every 10,000 s followed by the CV cleaning. Three cycles of 10,000 s were examined. The liquid products were analyzed by using HPLC (Agilent, 1260 Infinity-II) equipped with Hi-Plex H columns. Upon the completion of electrolysis at 0.85 and 1.05 V_{RHE} for 1 h, 1.5 mL electrolyte was collected for HPLC analysis. The faradaic efficiency of acetic acid was calculated by the ratio of the number of electrons consumed toward CH_3COOH to the number of electrons passing through the working electrode. The IRRAS tests were performed on the Nicolet IS50 spectrometer equipped with a mercuric cadmium telluride detector. The homemade electrochemical cell was used, including a ZnSe hemisphere window, an Au working electrode, an Ag/AgCl reference electrode, and a Pt wire counter electrode (30). The IRRAS spectra were obtained in the 0.1 M $HClO_4$ and 0.2 M C_2H_5OH solution from 0.05 to 1.05 V. The 127 interferograms were used in the test with the 4 cm^{-1} of resolution. The obtained spectra were postprocessed by subtracting the first reference spectrum. The selectivity for each of the EOR products were calculated by the following equation:

$$\text{Selectivity}(\%) = \frac{n_i\, Q_i}{\sum n_i\, Q_i} \quad Q\ (\text{mol cm}^{-2}) = \frac{A_i}{\varepsilon_{eff}},$$

in which A_i is the integrated band intensities, ε_{eff} is the effective absorption coefficient taken from the work of Weaver and coworkers (31, 32), and n_i is the transferred electron numbers from ethanol to the respective product.

XAFS Analysis. The XAFS analysis was conducted on the 7-BM (QAS) beamline at National Synchrotron Light Source-II in Brookhaven National Laboratory (BNL). The obtained spectra were processed using the IFFEFFIT package (33, 34). For the EXAFS analysis, the original EXAFS pattern [χ(k)] was weighted with k^3 in order to intensify the high-k oscillation regime and was Fourier transformed using a Hanning window. The amplitude reduction factor (S_O^2) was attained from the corresponding foil. All of the EXAFS fittings were done in the R space. All fitting parameters and results are tabulated in *SI Appendix*, Tables S2–S6.

In situ XAFS analysis was conducted on the 7D (XAFS) beamline at Pohang Light Source in the Pohang Accelerating Laboratory. The XAFS signal was

recorded with fluorescent mode by using a seven-channel germanium (Ge) detector mainly because of the diluted amount of Rh in the samples. The laboratory-made acryl kit was used as described in our previous work (35). The areal loading of the working electrode was c.a. 3 mg · cm^{-2}. During the measurement, Ar gas was continuously bubbled into the electrolyte. The working electrode potential was controlled by an RHE (Hydroflex, EDAQ), and graphite paper (highly oriented pyrolytic graphite) was used as a counter electrode. The other conditions were similar to the electrochemical operation except for the ethanol concentration (1 M) in order to compensate the higher mass loading of the working electrode.

Computational Methods. Spin-polarized DFT (36, 37) calculations were performed at a generalized gradient approximation (38) level using the plane wave Vienna Ab-Initio Simulation Package code (39, 40). The core electrons were described using the projector augmented wave (41) potentials using PW91 functionals (42). A kinetic energy cutoff of 400 eV and 3 × 3 × 1 k-point mesh were used in all structure optimization calculations.

The Pt(100) surface was modeled using a four-layer 3 × 3 surface slab. Rh_{at}-Pt NCs in our DFT calculations were represented by an Rh atom adsorbed at the most favorable site on ML O-covered Pt(100). Rh single-atom adsorbed on Pt(100) namely Rh_{at}-Pt(100) was modeled to represent the Rh single-atom catalyst without surface O on the Pt surface. A vacuum layer of ∼15 Å thick was added in the slab cell along the direction perpendicular to the surface to minimize the artificial interactions between the surface and its periodic images. Atoms in the bottom two layers were fixed, while all other atoms were allowed to relax during geometry optimization until the Hellmann–Feynman force on each ion was smaller than 0.02 eV · $Å^{-1}$.

The BE of adsorbate was calculated as the following:

$$BE(adsorbate) = E(slab + adsorbate) - E(slab) - E(adsorbate),$$

in which E(slab + adsorbate), E(slab), and E(adsorbate) are the total energies of the slab with adsorbate, clean slab, and adsorbate species in the gas phase, respectively.

The free energy change (ΔG) along various reaction pathways was calculated using the approach developed by Nørskov and coworkers (43). In this approach, the free energy of adsorbed species at applied potential (U) = 0 V is calculated as the following:

$$G(adsorbed\ species) = E_{DFT} + ZPE - TS$$

in which E_{DFT} is the DFT calculated total energy of adsorbed species, ZPE is the zero-point energy, and TS is the entropic corrections (*SI Appendix*, Table S10).

Activation energy calculations were performed using the climbing image nudged elastic band method (44).

Data Availability. All study data are included in the article and/or *SI Appendix*.

ACKNOWLEDGMENTS. Those of us at Columbia University acknowledge support by the US Department of Energy (DOE), Office of Basic Energy Sciences, Catalysis Science Program (Grant No. DE-FG02-13ER16381). Those of us at Kyungpook National University acknowledge support by the National Research Foundation of Korea (NRF-2021R1A2C4001411, NRF-2021R1G1A1092280, and NRF-2020R1A4A1018393). Those of us at the University of California San Diego acknowledge support from the American Chemical Society Petroleum Research Fund (No. 59989-DNI5) and the startup fund from the Jacob School of Engineering. DFT calculations were performed using computational resources at the Extreme Science and Engineering Discovery Environment, which is supported by the NSF Grant No. ACI-1548562. This research used resources of the Center for Functional Nanomaterials, which is a US DOE Office of Science Facility, and the Scientific Data and Computing Center, a component of the BNL Computational Science Initiative, at BNL under Contract No. DE-SC0012704. This research used resources at the 7-BM (QAS) beamline of the National Synchrotron Light Source-II at BNL and 7D (XAFS) beamline of the Pohang Light Source-II at the Pohang Accelerating Laboratory. The QAS operations were supported in part by the Synchrotron Catalysis Consortium under US DOE, Office of Basis Energy Sciences under Grant No. DE-SC0012653.

Author affiliations: [a]Department of NanoEngineering, University of California San Diego, La Jolla, CA 92093; [b]Department of Chemical Engineering, Columbia University, New York, NY 10027; [c]Department of Chemistry and Green-Nano Materials Research Center, Kyungpook National University, Daegu 41566, Republic of Korea; [d]School of Materials Science and Engineering, Kyungpook National University, Daegu 41566, Republic of Korea; [e]Department of Physics, Florida A&M University, Tallahassee, FL 32307; [f]Center for Functional Nanomaterials, Brookhaven National Laboratory, Upton, NY 11973; [g]Department of Chemistry, University of Ulsan, Ulsan 44776, Republic of Korea; [h]Program of Chemical Engineering, University of California San Diego, La Jolla, CA 92093; [i]Chemistry Division, Brookhaven National Laboratory, Upton, NY 11973; and [j]Department of Hydrogen and Renewable Energy, Kyungpook National University, Daegu 41566, Republic of Korea

1. N. Marković, T. Schmidt, V. Stamenković, P. Ross, Oxygen reduction reaction on Pt and Pt bimetallic surfaces: A selective review. *Fuel Cells (Weinh.)* **1**, 105–116 (2001).
2. J. Zhang *et al.*, Platinum monolayer electrocatalysts for O_2 reduction: Pt monolayer on Pd (111) and on carbon-supported Pd nanoparticles. *J. Phys. Chem. B* **108**, 10955–10964 (2004).
3. R. Adzic, *Recent advances in the kinetics of oxygen reduction. Technical Report* (Department of Energy, United States, 1996).
4. M. Scohy *et al.*, Investigating the oxygen evolution reaction on Ir (111) electrode in acidic medium using conventional and dynamic electrochemical impedance spectroscopy. *Electrochim. Acta* **320**, 134536 (2019).
5. A. Chen, J. Lipkowski, Electrochemical and spectroscopic studies of hydroxide adsorption at the Au (111) electrode. *J. Phys. Chem. B* **103**, 682–691 (1999).
6. Q. Chang *et al.*, Boosting activity and selectivity of CO_2 electroreduction by pre-hydridizing Pd nanocubes. *Small* **16**, e2005305 (2020).
7. Q. Chang *et al.*, Enhancing C–C bond scission for efficient ethanol oxidation using PtIr nanocube electrocatalysts. *ACS Catal.* **9**, 7618–7625 (2019).
8. Q. Chang *et al.*, Structural evolution of sub-10 nm octahedral platinum–nickel bimetallic nanocrystals. *Nano Lett.* **17**, 3926–3931 (2017).
9. Q. Chang *et al.*, Promoting H_2O_2 production via 2-electron oxygen reduction by coordinating partially oxidized Pd with defect carbon. *Nat. Commun.* **11**, 2178 (2020).
10. X. Ao *et al.*, Atomically dispersed Fe–N–C decorated with Pt-alloy core–shell nanoparticles for improved activity and durability towards oxygen reduction. *Energy Environ. Sci.* **13**, 3032–3040 (2020).
11. X. Huang *et al.*, High-performance transition metal–doped Pt_3Ni octahedra for oxygen reduction reaction. *Science* **348**, 1230–1234 (2015).
12. Z. Li *et al.*, Iridium single-atom catalyst on nitrogen-doped carbon for formic acid oxidation synthesized using a general host-guest strategy. *Nat. Chem.* **12**, 764–772 (2020).
13. A. Han *et al.*, Recent advances for MOF-derived carbon-supported single-atom catalysts. *Small Methods* **3**, 1800471 (2019).
14. C. H. Choi *et al.*, The Achilles' heel of iron-based catalysts during oxygen reduction in an acidic medium. *Energy Environ. Sci.* **11**, 3176–3182 (2018).
15. S. Luo *et al.*, A tensile-strained Pt–Rh single-atom alloy remarkably boosts ethanol oxidation. *Adv. Mater.* **33**, e2008508 (2021).
16. E. A. Monyoncho *et al.*, Ethanol electro-oxidation on palladium revisited using polarization modulation infrared reflection absorption spectroscopy (PM-IRRAS) and density functional theory (DFT): Why is it difficult to break the C–C bond? *ACS Catal.* **6**, 4894–4906 (2016).
17. S. Xie *et al.*, Atomic layer-by-layer deposition of Pt on Pd nanocubes for catalysts with enhanced activity and durability toward oxygen reduction. *Nano Lett.* **14**, 3570–3576 (2014).
18. K. Wade, Metal-metal and metal-carbon bond energy terms for the rhodium carbonyl clusters $Rh_4(CO)_{12}$ and $Rh_6(CO)_{16}$. *Inorg. Nucl. Chem. Lett.* **14**, 71–74 (1978).
19. T. J. P. Hersbach, R. Kortlever, M. Lehtimäki, P. Krtil, M. T. M. Koper, Local structure and composition of PtRh nanoparticles produced through cathodic corrosion. *Phys. Chem. Chem. Phys.* **19**, 10301–10308 (2017).
20. N. Markovic, H. Gasteiger, P. N. Ross, Kinetics of oxygen reduction on Pt (hkl) electrodes: Implications for the crystallite size effect with supported Pt electrocatalysts. *J. Electrochem. Soc.* **144**, 1591–1597 (1997).
21. A. Kowal *et al.*, Ternary Pt/Rh/SnO_2 electrocatalysts for oxidizing ethanol to CO_2. *Nat. Mater.* **8**, 325–330 (2009).
22. L.-W. H. Leung, S.-C. Chang, M. J. Weaver, Real-time FTIR spectroscopy as an electrochemical mechanistic probe: Electrooxidation of ethanol and related species on well-defined Pt (111) surfaces. *J. Electroanal. Chem. Interfacial Electrochem.* **266**, 317–336 (1989).
23. Y. Qu *et al.*, Quantitative pinhole on-line electrochemical mass spectrometry study on ethanol electro-oxidation at carbon-supported Pt and Ir-containing catalysts. *Int. J. Hydrogen Energy* **42**, 228–235 (2017).
24. F. Colmati *et al.*, Surface structure effects on the electrochemical oxidation of ethanol on platinum single crystal electrodes. *Faraday Discuss.* **140**, 379–397 (2008).
25. N. Binsted, S. L. Cook, J. Evans, G. N. Greaves, R. J. Price, EXAFS and near-edge structure in the cobalt K-edge absorption spectra of metal carbonyl complexes. *J. Am. Chem. Soc.* **109**, 325–330 (1987).
26. I. R. Beattie, P. J. Jones, N. A. Young, Characterization of some novel first row transition metal carbonyl chlorides by infrared and EXAFS spectroscopy of matrix-isolated species. *J. Am. Chem. Soc.* **114**, 6146–6152 (1992).
27. N. Binsted, J. Evans, G. N. Greaves, R. J. Price, Characterization of supported rhodium and ruthenium carbonyl clusters by EXAFS spectroscopy. *Organometallics* **8**, 613–620 (1989).
28. Z. Xie *et al.*, Reactions of CO_2 and ethane enable CO bond insertion for production of C3 oxygenates. *Nat. Commun.* **11**, 1887 (2020).
29. J. Zhang *et al.*, Ethanol steam reforming on Rh catalysts: Theoretical and experimental understanding. *ACS Catal.* **4**, 448–456 (2014).
30. Z. Jiang, Q. Zhang, Z. Liang, J. G. Chen, Pt-modified TaC as an efficient electrocatalyst for ethanol oxidation in acid and alkaline electrolytes. *Appl. Catal. B* **234**, 329–336 (2018).
31. P. Gao, S.-C. Chang, Z. Zhou, M. J. Weaver, Electrooxidation pathways of simple alcohols at platinum in pure nonaqueous and concentrated aqueous environments as studied by real-time FTIR spectroscopy. *J. Electroanal. Chem. Interfacial Electrochem.* **272**, 161–178 (1989).
32. M. Weaver *et al.*, Evaluation of absolute saturation coverages of carbon monoxide on ordered low-index platinum and rhodium electrodes. *J. Electroanal. Chem. (Lausanne)* **327**, 247–260 (1992).

33. B. Ravel, M. Newville, ATHENA, ARTEMIS, HEPHAESTUS: Data analysis for X-ray absorption spectroscopy using IFEFFIT. *J. Synchrotron Radiat.* **12**, 537–541 (2005).
34. J. J. Rehr, R. C. Albers, Theoretical approaches to X-ray absorption fine structure. *Rev. Mod. Phys.* **72**, 621 (2000).
35. J. H. Lee *et al.*, Tuning the activity and selectivity of electroreduction of CO_2 to synthesis gas using bimetallic catalysts. *Nat. Commun.* **10**, 3724 (2019).
36. P. Hohenberg, W. Kohn, Density functional theory (DFT). *Phys. Rev.* **136**, B864 (1964).
37. W. Kohn, L. Sham, Self-consistent equations including exchange and correlation effects. *Phys. Rev.* **140**, 1 (1965).
38. J. P. Perdew, K. Burke, M. Ernzerhof, Perdew, burke, and ernzerhof reply. *Phys. Rev. Lett.* **80**, 891 (1998).
39. G. Kresse, J. Furthmüller, Efficiency of ab-initio total energy calculations for metals and semiconductors using a plane-wave basis set. *Comput. Mater. Sci.* **6**, 15–50 (1996).
40. G. Kresse, J. Hafner, Ab initio molecular dynamics for open-shell transition metals. *Phys. Rev. B Condens. Matter* **48**, 13115–13118 (1993).
41. P. E. Blöchl, Projector augmented-wave method. *Phys. Rev. B Condens. Matter* **50**, 17953–17979 (1994).
42. J. P. Perdew, Y. Wang, Pair-distribution function and its coupling-constant average for the spin-polarized electron gas. *Phys. Rev. B Condens. Matter* **46**, 12947–12954 (1992).
43. J. K. Nørskov *et al.*, Origin of the overpotential for oxygen reduction at a fuel-cell cathode. *J. Phys. Chem. B* **108**, 17886–17892 (2004).
44. G. Henkelman, B. P. Uberuaga, H. Jónsson, A climbing image nudged elastic band method for finding saddle points and minimum energy paths. *J. Chem. Phys.* **113**, 9901–9904 (2000).